

Article

The Synthesis of Metal–Organic-Framework-Based Ternary Nanocomposite for the Adsorption of Organic Dyes from Aqueous Solutions

Norah Salem Alsaari ¹, Haitham Osman ², Abdelfattah Amari ^{2,3,*} and Mohamed A. Tahooun ^{4,5}

¹ Department of Chemistry, College of Science, Princess Nourah bint Abdulrahman University, P.O. Box 84428, Riyadh 11671, Saudi Arabia

² Department of Chemical Engineering, College of Engineering, King Khalid University, Abha 61411, Saudi Arabia

³ Research Laboratory of Processes, Energetics, Environment and Electrical Systems, National School of Engineers, Gabes University, Gabes 6072, Tunisia

⁴ Department of Chemistry, College of Science, King Khalid University, P.O. Box 9004, Abha 61413, Saudi Arabia

⁵ Chemistry Department, Faculty of Science, Mansoura University, Mansoura 35516, Egypt

* Correspondence: abdefattah.amari@enig.rnu.tn

Abstract: In the present study, a ternary magnetic nanocomposite (SiO₂/MnFe₂O₄/ZIF-8) was synthesized via the embedding of the SiO₂/MnFe₂O₄ nanocomposite within the metal–organic framework (ZIF-8). The synthesized nanocomposite was characterized using suitable techniques including FT-IR, XRD, SEM, TEM, VSM, and BET. The nanocomposite showed a high surface area (S_{BET} = 831 m²·g^{−1}) and superparamagnetic behavior (23.7 emu·g^{−1}). All characterization techniques confirmed the successful combination of three nanocomposite parts (MnFe₂O₄, SiO₂, and ZIF-8). The nanocomposite was examined for the adsorption of organic dyes, malachite green (MG) and methyl red (MR), from aqueous solutions. The adsorption conditions including ionic strength, contact time, pH, and adsorbent dosage were optimized by studying their change effect. The SiO₂/MnFe₂O₄/ZIF-8 nanocomposite showed high adsorption capacities (1000.03 and 1111.12 mg/g) for the removal of MG and MR, respectively, from water. The isotherm and kinetics studies indicated that the adsorption of MG and MR dyes on the surface of the SiO₂/MnFe₂O₄/ZIF-8 nanocomposite followed the Langmuir isotherm model and pseudo-second-order kinetic model, suggesting the monolayer chemisorption mechanism. The reusability study of up to five successive cycles indicated the successful reuse of the SiO₂/MnFe₂O₄/ZIF-8 adsorbent for dye removal from wastewater. The comparison of the present adsorbent to the previously reported adsorbents indicated that it is a promising adsorbent for dye adsorption from wastewater and must be investigated in the future for the removal of additional pollutants.

Keywords: dye adsorption; water treatment; nanomaterials; metal-organic framework



Citation: Alsaari, N.S.; Osman, H.; Amari, A.; Tahooun, M.A. The Synthesis of Metal–Organic-Framework-Based Ternary Nanocomposite for the Adsorption of Organic Dyes from Aqueous Solutions. *Magnetochemistry* **2022**, *8*, 133. <https://doi.org/10.3390/magnetochemistry8100133>

Academic Editors: Wei Ding and Huaili Zheng

Received: 25 September 2022

Accepted: 17 October 2022

Published: 19 October 2022

Publisher's Note: MDPI stays neutral with regard to jurisdictional claims in published maps and institutional affiliations.



Copyright: © 2022 by the authors. Licensee MDPI, Basel, Switzerland. This article is an open access article distributed under the terms and conditions of the Creative Commons Attribution (CC BY) license (<https://creativecommons.org/licenses/by/4.0/>).

1. Introduction

Nowadays, water pollution represents a major problem in the world [1,2]. Dyes, heavy metals, and herbicides are the most common biological, inorganic, and organic pollutants in water and soil [3]. Among all water-existing pollutants, dyes are the most harmful species to the environment [4]. For example, methyl red (MR) and malachite green (MG) are widely used in different daily activities such as cosmetics, paper industries, food industries, printing, and textiles [5,6]. The release of such dyes may lead to serious problems for human health or the environment due to their high toxicity, mutagenic effect, and carcinogenic effect [7,8]. MR dye has an accumulative tendency due to its low bio-degradability resulting from the existence of a benzene ring in addition to its mutagenic effect under aerobic environments [9]. In addition, MR can cause digestive tract damage, and skin and eye irritations [10]. MG

dye has a mutagenic effect and carcinogenic effect, and can cause damage to the human respiratory system [11]. According to reports from the World Health Organization (WHO), environmental contaminants found in the soil, air, and water cause 25% of human health diseases [12]. Subsequently, these dyes must be treated before being released into the environment. Efforts have been made to develop a rapid, suitable, and effective method for the removal of dyes from wastewater. The decolorization of dyes has been achieved via several technologies including ion-exchange [13], reverse osmosis [14], precipitation [15], degradation [16,17], coagulation [18,19], and adsorption [20–23]. Among all used technologies, adsorption is the widely used method for dye removal due to the availability of a large number of adsorbents, its effectiveness, simple operation, low cost, and versatility [24]. Additionally, the adsorption method is used to separate dyes from waste on an industrial level. However, classical adsorbents such as zeolite, silica, and carbon have several limitations including the requirement of a long contact time, low adsorption capacity, difficult regeneration process, and the resultant secondary pollution [25]. Thus, the magnetic separation methods and large surface adsorbents have attracted attention to avoid secondary pollution and enhance the adsorption capacity in addition to the fast processing and ease of reusability and regeneration [26,27]. For example, different adsorbents have been magnetized for the effective removal of water pollutants such as a magnetic carbonaceous adsorbent for the removal of methylene violet [28], a $\text{FeNi}_3/\text{SiO}_2/\text{CuS}$ nanocomposite for the removal of Congo red dye [29], a magnetic-polymer-based nanocomposite for the removal of Congo red dye and hexavalent chromium Cr(VI) ions [30], and a magnetic-lignin-based adsorbent for the removal of several azo dyes [31].

Recently, the attractive properties of metal–organic frameworks (MOFs) have attracted scientists' attention for application in different fields [32,33]. MOFs are known as porous coordination polymers with magnificent properties that have allowed their use in different fields of application including heterogeneous catalysis [34], adsorptive removal of toxic species [35], membranes [36], magnetism [37], luminescence [38], sensors [39], storage of gases [40], photocatalysis [41], ion exchange [42], and drug delivery [43].

MOFs are formed from inorganic clusters as building blocks and linkers of organic ligands to produce an organic–inorganic hybrid of porous architectures [44]. This mixing of inorganic and organic moieties resulted in the synthesis of more than 10,000 MOF constructions [45]. MOFs have a 3-D network with a high pore volume, homogenous micropores, and a large surface area. The change in inorganic clusters and organic linkers is used to turn their shape and pore size from a microporous to a mesoporous scale that gives them specific attention [46]. MOFs showed an improved adsorption capacity and selectivity toward different pollutants due to the presence of open sites in their structures. These advantages of MOFs including large surface area, tunable pore size, and composition diversity [47] allowed their use as adsorbents for the removal of different types of pollutants such as benzene [48], naphthalene [49], dyes [50], and sulfur compounds [51]. However, MOFs have the limitation of difficult separation from aqueous solutions that hinder their application as adsorbents. This limitation can be overcome through the magnetization of MOF_5 allowing their separation by applying an external magnetic field. The magnetization of MOF_5 by filling it with magnetic nanomaterials produces a composite with high adsorption capacity to remove organic dyes from an aqueous solution, and it is also simpler to separate from an adsorption environment that prevents secondary pollution. Recent works have reported the magnetization of MOFs for the efficient removal of water pollutants such as MIL-101(Fe) modified with magnetic Fe_3O_4 for the removal of malachite green and methyl red [52], a $\text{Fe}_3\text{O}_4@\text{MIL-100(Fe)}$ composite for the degradation of methylene blue [53], and magnetic amino-functionalized $\text{La-MOF (MOF/NH}_2/\text{Fe}_3\text{O}_4)$ for the removal of methyl orange dye [54]. These magnetic MOFs showed many advantages such as retaining excellent performance up to several consecutive cycles, exhibiting a significant adsorbent potential, and the ability to be easily removed from liquid media.

In this work, the ZIF-8 MOF as zeolitic imidazolate frameworks was synthesized and embedded with $\text{SiO}_2/\text{MnFe}_2\text{O}_4$ nanoparticles to produce a nanocomposite named

$\text{SiO}_2/\text{MnFe}_2\text{O}_4/\text{ZIF-8}$. The synthesized nanocomposite was characterized using proper techniques including Fourier-transform infrared spectroscopy (FTIR), X-ray diffraction (XRD), transmission electron microscopy (TEM), a scanning electron microscope (SEM), BET, and a vibrating sample magnetometer (VSM). Then, the efficiency of the synthesized adsorbent for the adsorption of MG and MR dyes from aqueous solution was evaluated and optimized by studying the effect of contact time, adsorbent dose, pH, and ionic strength. Additionally, pseudo-first-order and second-order models were used to study the adsorption kinetics. Finally, Langmuir and Freundlich isotherm models were used to study the adsorption mechanism. The reusability of the $\text{SiO}_2/\text{MnFe}_2\text{O}_4/\text{ZIF-8}$ nanocomposite for the removal of MG and MR dyes was studied by applying an external magnet. The possibility of using the $\text{SiO}_2/\text{MnFe}_2\text{O}_4/\text{ZIF-8}$ nanocomposite as an adsorbent for dye removal from an aqueous solution was finally assessed.

2. Materials and Methods

2.1. Chemicals

All reagents were analytical grade and used without any purifications. Tetraethyl orthosilicate (TEOS), 2-methylimidazole, manganese nitrate, iron nitrate, methyl red (MR), malachite green (MG), and zinc nitrate were supplied from Sigma-Aldrich, Germany. Ethyl alcohol, Ethylene Diamine (EDA), aqueous ammonia, hydrochloric acid, and sodium hydroxide were supplied from Elgomhoria Chemical Co, Cairo, Egypt. All solutions were prepared using distilled water.

2.2. Synthesis of $\text{SiO}_2/\text{MnFe}_2\text{O}_4$ Nanocomposite

For the synthesis of the $\text{SiO}_2/\text{MnFe}_2\text{O}_4$ nanocomposite, MnFe_2O_4 nanoparticles were synthesized first using a co-precipitation process as reported in the literature [55]. In a typical method, a mixed solvent of 3.0 mL of EDA and 70.0 mL of distilled H_2O was used to dissolve 4.20 g of NaOH followed by the addition of 4.9 g of manganese nitrate and 13.4 g of iron nitrate that previously dissolved in 50.0 mL of distilled H_2O . To reach the complete complexation, the previous mixture was heated for 3 h at 100 °C. After that, the synthesized magnetic MnFe_2O_4 nanoparticles were collected using an external magnet and washed many times using H_2O and ethyl alcohol followed by the dryness of nanoparticles at room temperature. Secondly, the modified Stöber process was used for the modification of MnFe_2O_4 nanoparticles using SiO_2 as reported in the literature [56]. Typically, a mixed solution of aqueous ammonia (1.2 mL, 25%), 20 mL of deionized H_2O , and ethyl alcohol (40 mL, 99.9%) was used to disperse MnFe_2O_4 nanoparticles (0.15 g) under ultrasonication for 60 min followed by the stepwise addition of TEOS (0.6 mL). The reaction was kept for up to 6 h at 30 °C followed by the separation of the synthesized $\text{SiO}_2/\text{MnFe}_2\text{O}_4$ nanocomposite using an external magnet. The collected nanocomposite was washed several times using ethyl alcohol and finally dried at 60 °C in a vacuum.

2.3. Synthesis of $\text{SiO}_2/\text{MnFe}_2\text{O}_4/\text{ZIF-8}$ Nanocomposite

The synthesis of the $\text{SiO}_2/\text{MnFe}_2\text{O}_4/\text{ZIF-8}$ nanocomposite was achieved as detailed in this section. First, the methanol solvent (65 mL) was used to disperse the $\text{SiO}_2/\text{MnFe}_2\text{O}_4$ nanocomposite (0.2 g) and zinc nitrate hexahydrate (2 mmol) under ultrasonication. After that, methanol (30 mL) was used to dissolve 2-methylimidazole (10 mmol) that was stepwise-added to the previous suspension at ambient temperature in a rotatory evaporator under strong stirring. Then, this produced mixture was kept for 1 day at room temperature to give grey powder of $\text{SiO}_2/\text{MnFe}_2\text{O}_4/\text{ZIF-8}$ that was collected using an external magnet. Finally, the synthesized nanocomposite was washed several times with ethyl alcohol and deionized H_2O and dried at 60 °C in a vacuum. Figure 1 illustrates the synthesis procedures of the $\text{SiO}_2/\text{MnFe}_2\text{O}_4/\text{ZIF-8}$ nanocomposite.

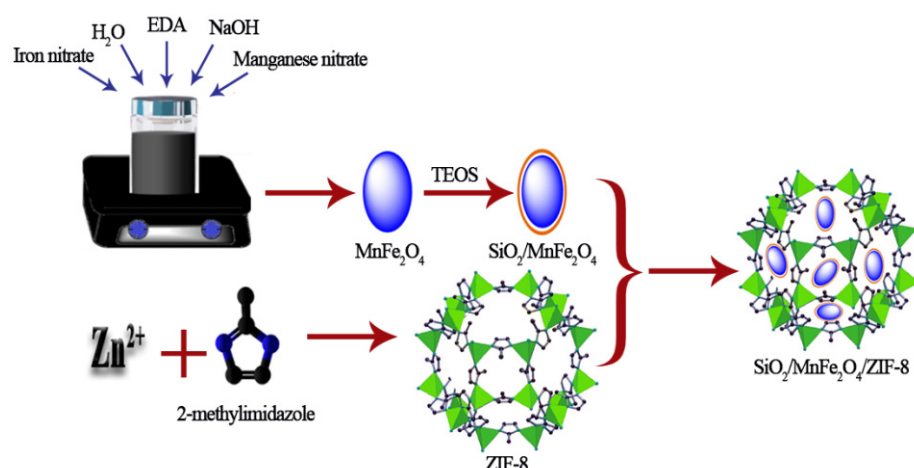


Figure 1. The synthesis scheme of $\text{SiO}_2/\text{MnFe}_2\text{O}_4/\text{ZIF-8}$ nanocomposite. (TEOS: Tetraethyl orthosilicate).

2.4. Adsorption Experiments

The synthesized $\text{SiO}_2/\text{MnFe}_2\text{O}_4/\text{ZIF-8}$ nanocomposite was evaluated for the adsorption of MG and MR dyes from an aqueous solution. First, deionized H_2O was used for the preparation of the required concentrations of the dyes. The batch adsorption experiments were performed by shaking 50.0 mL of dye solution (50.0 to 500.0 mg/L) with 0.01 g of the adsorbent using a water bath shaker at 250 rpm at 25 °C and the required pH value. The shaking process was continued until reaching equilibrium, which was 60 min for MG and 30 min for MR. The best conditions of the adsorption process were performed by studying the effect of pH, contact time, adsorbent dose, and ionic strength. The effect of pH was investigated in the range of 3–12. The pH values were adjusted using the buffer solution and the measurements were carried out using a digital pH meter. To study the effect of contact time, the adsorption experiments were performed at different time intervals ranging from 0 to 240 min. To study the ionic strength effect, different concentrations of NaCl salt were added to the water samples in the range of 0–0.5 M. To study the effect of adsorbent dose, the adsorption experiments were performed using different masses of adsorbent in the range of 0.15–1 g/L. After each adsorption experiment, the adsorbent was collected using an external magnet and the supernatant was examined for the existence of the MG and MR dyes using a UV-Vis spectrophotometer at $\lambda = 620$ nm and 526 nm, respectively. The adsorption capacity at equilibrium (q_e , mg/g) of the $\text{SiO}_2/\text{MnFe}_2\text{O}_4/\text{ZIF-8}$ nanocomposite was calculated according to Equation (1).

$$q_e = (C_o - C_e)V/m \quad (1)$$

where m , V , C_e , and C_o are the mass of the adsorbent in g, the volume of the solution in L, the equilibrium concentration of the dye (mg/L), and the initial concentration of the dye (mg/L), respectively.

Moreover, the reusability of the $\text{SiO}_2/\text{MnFe}_2\text{O}_4/\text{ZIF-8}$ nanocomposite as an adsorbent for the removal of MG and MR dyes was investigated for up to five cycles. Each cycle consists of an adsorption process followed by the collection of adsorbent using a magnet for the desorption process to be used in the next cycle. The desorption process examined a mixed solvent of ethyl alcohol and H_2O with a ratio of 8:2, respectively. During each desorption process, the eluent was mixed with the eluent for half an hour with sonication followed by magnetic separation and dryness at 70 °C. After each cycle, the adsorbent was collected and the solution was examined for the presence of dyes. Finally, the regeneration and reusability of the $\text{SiO}_2/\text{MnFe}_2\text{O}_4/\text{ZIF-8}$ nanocomposite for dye removal were evaluated.

3. Results and Discussion

3.1. Characterization of Synthesized Nanomaterials

For the characterization of the synthesized nanomaterials, MnFe_2O_4 nanoparticles, the $\text{SiO}_2/\text{MnFe}_2\text{O}_4$ nanocomposite, and the $\text{SiO}_2/\text{MnFe}_2\text{O}_4/\text{ZIF-8}$ nanocomposite, the proper techniques were used, as discussed in this section. TEM and SEM images were used for the identification of particle size and surface morphology, as shown in Figure 2. Figure 2a shows the TEM image of MnFe_2O_4 nanoparticles indicating the nanosize of the synthesized magnetic particles. Figure 2b shows the TEM image of the $\text{SiO}_2/\text{MnFe}_2\text{O}_4$ nanocomposite that clearly showed the good addition of SiO_2 to the magnetic MnFe_2O_4 nanoparticles. Figure 2c shows the TEM image of the $\text{SiO}_2/\text{MnFe}_2\text{O}_4/\text{ZIF-8}$ nanocomposite that showed the good dispersion of the $\text{SiO}_2/\text{MnFe}_2\text{O}_4$ nanocomposite inside the structure of ZIF-8 nanostructures. Moreover, the size and morphology of synthesized nanomaterials were confirmed using SEM images. Figure 2d shows the SEM image of the synthesized magnetic MnFe_2O_4 nanoparticles, confirming the nanoscale size of the particles with agglomeration tendency due to the magnetic behavior. Figure 2e shows the SEM image of the $\text{SiO}_2/\text{MnFe}_2\text{O}_4$ nanocomposite with a larger size than MnFe_2O_4 nanoparticles due to the addition of the SiO_2 layer that confirms the TEM results. Additionally, Figure 2e indicates that the $\text{SiO}_2/\text{MnFe}_2\text{O}_4$ nanocomposite was uniform. Figure 2f shows the SEM image of the $\text{SiO}_2/\text{MnFe}_2\text{O}_4/\text{ZIF-8}$ nanocomposite, indicating the nanosize scale of the synthesized nanocomposite after the embedding of the $\text{SiO}_2/\text{MnFe}_2\text{O}_4$ nanocomposite inside the structure of ZIF-8. The $\text{SiO}_2/\text{MnFe}_2\text{O}_4/\text{ZIF-8}$ nanocomposite showed a wide size range distribution from 30.0 nm to 200.0 nm with a rhombic dodecahedral structure. The SEM and TEM images show that the $\text{SiO}_2/\text{MnFe}_2\text{O}_4$ nanocomposite was well encapsulated by a shell of ZIF-8.

XRD of the synthesized nanomaterials was performed to characterize the composition and crystallinity, and the results are shown in Figure 3a. The XRD of magnetic MnFe_2O_4 nanoparticles indicated the spinel structure of magnetic nanoparticles, as confirmed from the appearance of characteristic peaks at $2\theta = 62.30, 56.80, 53.33, 43.06, 35.37,$ and 30.02 , which correspond to the planes (440), (511), (422), (400), (311), and (220) [57]. From the XRD of the $\text{SiO}_2/\text{MnFe}_2\text{O}_4$ nanocomposite, the amorphous properties of SiO_2 did not change the phase of MnFe_2O_4 magnetic nanoparticles when added, as inferred from the identical XRD patterns. From the XRD of the $\text{SiO}_2/\text{MnFe}_2\text{O}_4/\text{ZIF-8}$ nanocomposite, new characteristic peaks of ZIF-8 appeared at $2\theta = 18.20, 16.54, 14.85, 13.00, 10.54,$ and 7.44 , which correspond to the planes (222), (013), (022), (112), (002), and (011) [58]. In addition, characteristic peaks of MnFe_2O_4 appeared in the XRD of the $\text{SiO}_2/\text{MnFe}_2\text{O}_4/\text{ZIF-8}$ nanocomposite. Thus, the XRD results indicated a good combination between the three parts of the nanocomposite MnFe_2O_4 , SiO_2 , and ZIF-8.

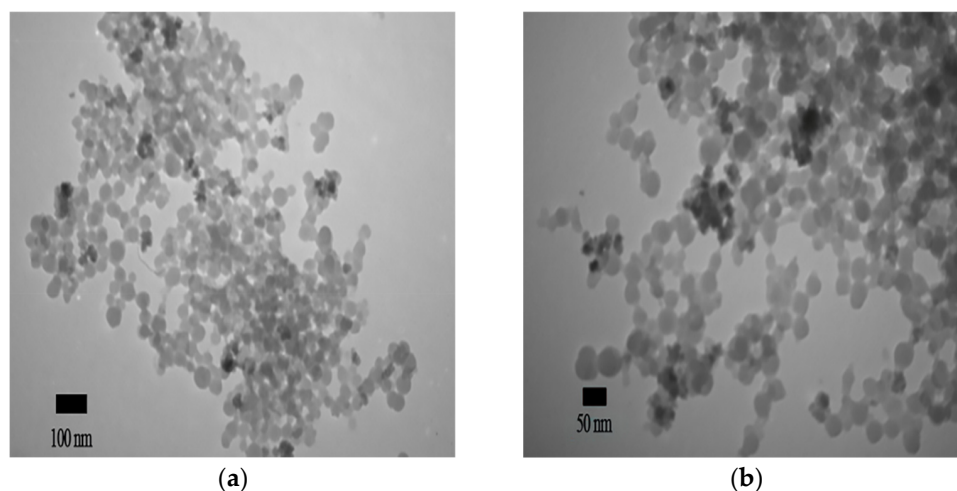


Figure 2. Cont.

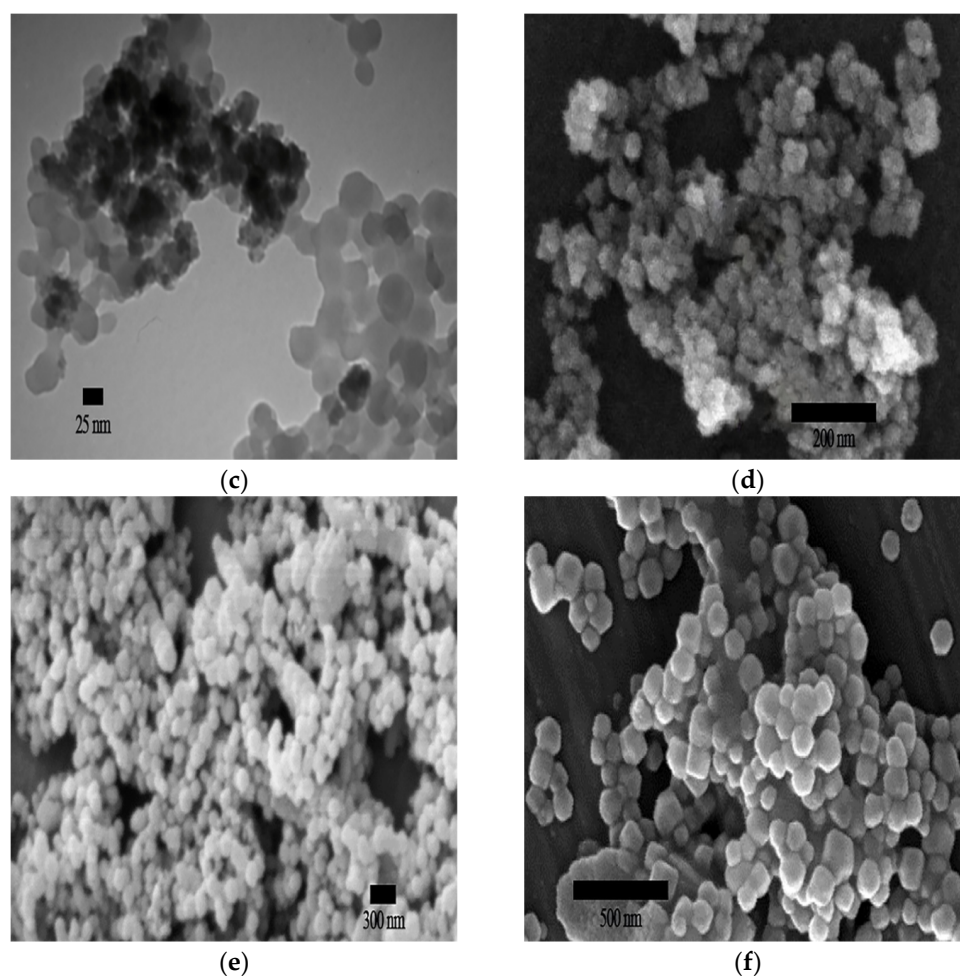


Figure 2. The TEM image of (a) MnFe_2O_4 nanoparticles, (b) $\text{SiO}_2/\text{MnFe}_2\text{O}_4$ nanocomposite, and (c) $\text{SiO}_2/\text{MnFe}_2\text{O}_4/\text{ZIF-8}$ nanocomposite, and SEM images of (d) MnFe_2O_4 nanoparticles, (e) $\text{SiO}_2/\text{MnFe}_2\text{O}_4$ nanocomposite, and (f) $\text{SiO}_2/\text{MnFe}_2\text{O}_4/\text{ZIF-8}$ nanocomposite.

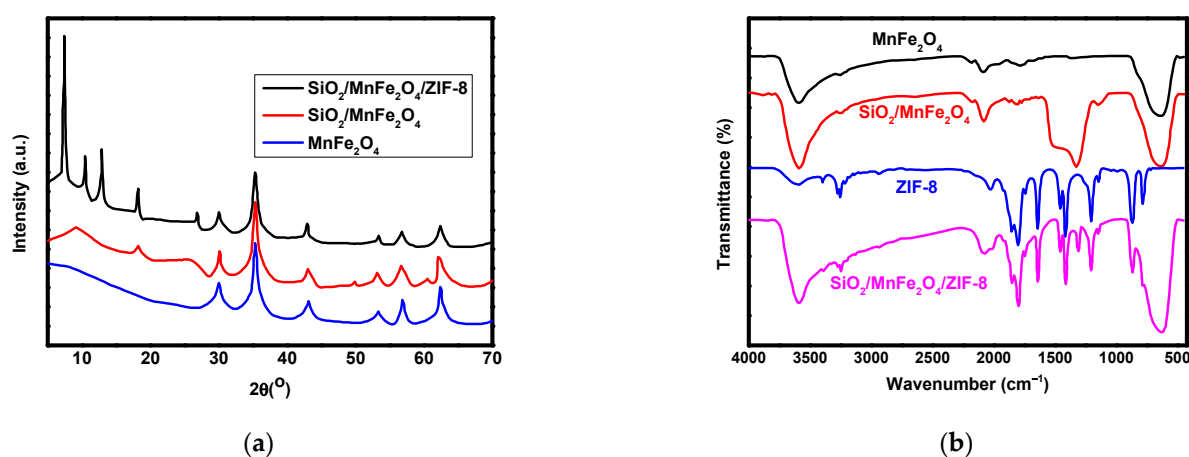


Figure 3. The XRD patterns (a) and FT-IR spectra (b) of the synthesized MnFe_2O_4 nanoparticles, $\text{SiO}_2/\text{MnFe}_2\text{O}_4$, and $\text{SiO}_2/\text{MnFe}_2\text{O}_4/\text{ZIF-8}$.

For the identification of functional groups, FT-IR spectra of the synthesized nanomaterials were generated in the range of $450\text{--}4000\text{ cm}^{-1}$, as shown in Figure 3b. According to Figure 3b, the MnFe_2O_4 nanoparticles showed an absorption band corresponding to the oxygen-metal bond at $500\text{--}600\text{ cm}^{-1}$ [59]. In addition, stretching vibrations of hydrogen-

bonded H–O groups showed an appearance of the minor band at 1620 cm^{-1} and the broad band at 3400 cm^{-1} [60]. The $\text{SiO}_2/\text{MnFe}_2\text{O}_4$ nanocomposite showed an absorption band corresponding to the OH–Si bond's bending vibration at 962 cm^{-1} , while the band corresponding to the Si–O–Si bond's asymmetric stretching vibration appeared at 1100 cm^{-1} – 1080 cm^{-1} [57]. The spectrum of the $\text{SiO}_2/\text{MnFe}_2\text{O}_4/\text{ZIF-8}$ nanocomposite showed the appearance of characteristic bands of ZIF-8. The hydroxyl groups of ZIF-8 and H_2O molecules showed the appearance of the band at 3430 cm^{-1} . The bands below 800 cm^{-1} were attributed to the out-of-plane bending of the ZIF-8 aromatic ring, while the in-plane bending bands were observed at the range of 950 – 1350 cm^{-1} . The vibration of the entire ring showed the appearance of bands in the range of 1550 – 1350 cm^{-1} . In addition, the stretching vibrations of the aliphatic chain of H-methylimidazole and aromatic ring C–H bonds showed the appearance of bands in the range of 2930 – 3135 cm^{-1} [61–63].

For the determination of magnetic properties, magnetization curves of the synthesized MnFe_2O_4 nanoparticles, $\text{SiO}_2/\text{MnFe}_2\text{O}_4$, and $\text{SiO}_2/\text{MnFe}_2\text{O}_4/\text{ZIF-8}$ were generated, as shown in Figure 4a. According to Figure 4a, all synthesized nanomaterials showed paramagnetic behavior with saturation values of 40.0, 33.8, and 23.7 emu/g for MnFe_2O_4 nanoparticles, $\text{SiO}_2/\text{MnFe}_2\text{O}_4$, and $\text{SiO}_2/\text{MnFe}_2\text{O}_4/\text{ZIF-8}$, respectively. The modification of magnetic MnFe_2O_4 nanoparticles with nonmagnetic SiO_2 caused a drop in saturation magnetization. In addition, the embedding of $\text{SiO}_2/\text{MnFe}_2\text{O}_4$ inside the ZIF-8 caused a drop in the saturation magnetization. However, the $\text{SiO}_2/\text{MnFe}_2\text{O}_4/\text{ZIF-8}$ nanocomposite still had good magnetic properties, allowing its magnetic separation by applying an external magnetic field. After the adsorption of dyes, the magnetic adsorbent could be collected using a magnet from the entire solution (Figure 4a, inset). This magnetic behavior of the adsorbent eases their reuse for water treatment, which reduces the overall cost of the treatment.

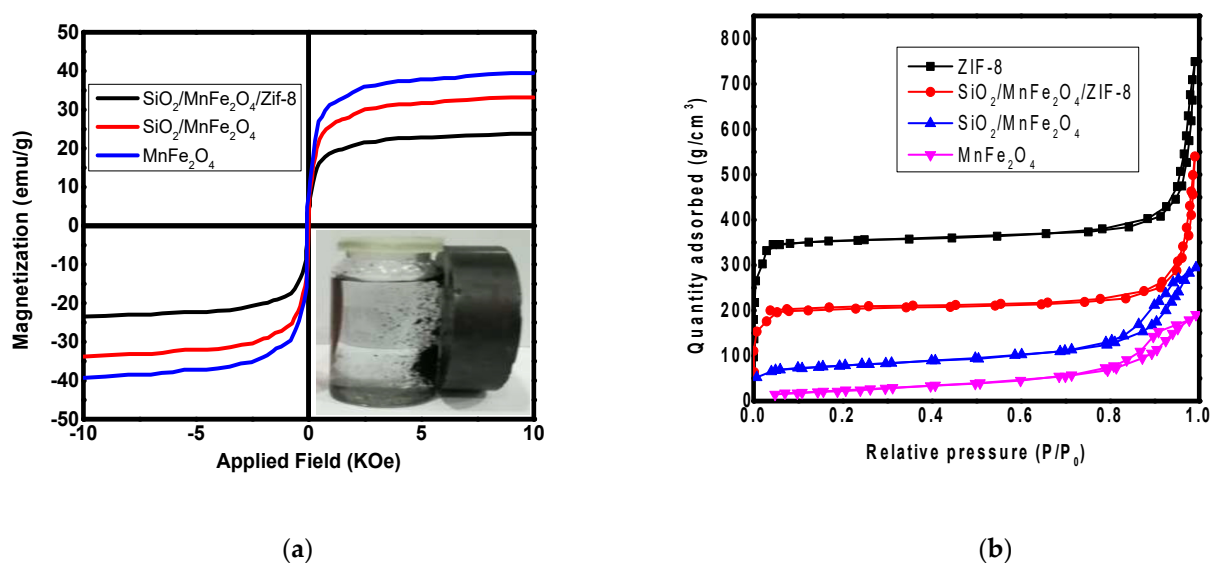


Figure 4. The magnetic curves (a) and N_2 adsorption–desorption isotherm (b) of the synthesized MnFe_2O_4 nanoparticles, $\text{SiO}_2/\text{MnFe}_2\text{O}_4$, and $\text{SiO}_2/\text{MnFe}_2\text{O}_4/\text{ZIF-8}$ (inset: a photograph for the magnetic separation of synthesized nanocomposite).

For the determination of specific surface area and porosity of synthesized nanomaterials, N_2 adsorption–desorption isotherms were measured, as shown in Figure 4b. According to Figure 4b, the $\text{SiO}_2/\text{MnFe}_2\text{O}_4/\text{ZIF-8}$ nanocomposite and ZIF-8 showed typical type I isotherms, indicating the microporous structure, while $\text{SiO}_2/\text{MnFe}_2\text{O}_4$ and MnFe_2O_4 nanoparticles are well known to have a mesoporous structure as they follow type IV isotherms with H3 hysteresis loops according to the literature [64]. The aggregation of magnetic MnFe_2O_4 nanoparticles made their pore diameter 12.6 nm and the adsorption to N_2 was weak. BET-specific surface areas (S_{BET}) were equal to $94\text{ m}^2\cdot\text{g}^{-1}$, $290\text{ m}^2\cdot\text{g}^{-1}$,

and $831 \text{ m}^2 \cdot \text{g}^{-1}$ for MnFe_2O_4 nanoparticles, the $\text{SiO}_2/\text{MnFe}_2\text{O}_4$ nanocomposite, and the $\text{SiO}_2/\text{MnFe}_2\text{O}_4/\text{ZIF-8}$ nanocomposite, respectively, indicating the enhanced surface area of the nanocomposite after embedding the $\text{SiO}_2/\text{MnFe}_2\text{O}_4$ nanocomposite inside the framework ZIF-8. This sharp increase in the surface area was attributed to the ideal structure of ZIF-8, which has a very high S_{BET} that is equal to $1485.5 \text{ m}^2 \cdot \text{g}^{-1}$. The characterization techniques indicated the successful combination between the three components SiO_2 , MnFe_2O_4 , and ZIF-8 to produce the $\text{SiO}_2/\text{MnFe}_2\text{O}_4/\text{ZIF-8}$ nanocomposite.

3.2. Optimization of the Adsorption Parameters

To determine the optimum conditions for the removal of MR and MG dyes on the surface of the $\text{SiO}_2/\text{MnFe}_2\text{O}_4/\text{ZIF-8}$ nanocomposite, the effects of different parameters including ionic strength, contact time, adsorbent dose, and pH were studied as shown in Figure 5. The effect of ionic strength on the removal of MR and MG dyes was studied using different NaCl concentrations ranging from 1×10^{-3} to 0.5 mol/L , as shown in Figure 5a. With a contact time of 60.0 min for the MG dye and 30.0 min for the MR dye, a stirring speed of 240 rpm at $25.0 \text{ }^\circ\text{C}$, an initial dye concentration of 100 ppm, and an adsorbent dose of 0.2 g/L , the influence of ionic strength on adsorption was investigated. According to Figure 5a, the adsorption capacity of MR and MG dyes was decreased by increasing the concentration of sodium chloride. This decrease in adsorption capacity associated with the increase in ionic strength is attributed to the decrease in electrostatic attraction between adsorbent and adsorbate. Additionally, the adsorbent molecules were agglomerated by increasing the ionic strength, causing a decrease in the number of adsorption sites [65]. In addition to this electrostatic influence, the salt ions could compete with the adsorbate ions for the adsorption sites, leading to the weakening of dye adsorption. The second studied parameter that affected the adsorption was the contact time. The adsorption of MR and MG dyes on the surface of the $\text{SiO}_2/\text{MnFe}_2\text{O}_4/\text{ZIF-8}$ nanocomposite was determined at a time ranging from 0 to 250 min, as shown in Figure 5b. According to Figure 5b, the adsorption capacity was increased up to 60 min for MG dye and 30 min for MR dye, and over this time, the adsorption capacity did not change. This increase in the adsorption capacity in the first stage was attributed to the availability of adsorption sites, until equilibrium was reached [66]. After that, there were unavailable adsorption sites to adsorb more ions of the dye due to the occupation of all adsorption sites causing no increase in the adsorption [67]. Subsequently, the optimum contact time was 60 min for MG dye and 30 min for MR dye, after which the adsorption became constant, revealing the saturation of active sites on the adsorbent surface.

Another significant parameter in the adsorption of dyes is the adsorbent dose. Figure 5c illustrates the effect of $\text{SiO}_2/\text{MnFe}_2\text{O}_4/\text{ZIF-8}$ dose on the removal of MG and MR dyes using 240 rpm as a stirring rate and 100 ppm as the initial dye concentration. According to Figure 5c, the adsorption capacity was sharply increased by increasing the adsorbent dose from 0.5 g/L to 0.2 g/L , after which the adsorption capacity declined. Subsequently, the optimum dose of $\text{SiO}_2/\text{MnFe}_2\text{O}_4/\text{ZIF-8}$ as the adsorbent was chosen as 0.2 g/L . This behavior could be attributed to the aggregation of adsorbent particles and overlapping of adsorption sites at a high dosage of the adsorbent, causing a decrease in the surface area and, correspondingly, a decrease in the adsorption capacity [68]. In addition, pH is a vital parameter affecting the adsorption of organic dyes. This importance arises from its effect on the ionization of both adsorbent surface and adsorbate molecules [69]. To study the effect of pH on the adsorption of MG and MR dyes on the surface of $\text{SiO}_2/\text{MnFe}_2\text{O}_4/\text{ZIF-8}$, experiments were examined in the pH range of 3 to 12, as shown in Figure 5d. The pH effect was determined at a stirring speed of 240 rpm and initial dye concentration of 100 ppm. According to Figure 5d, the increasing pH value caused a decrease in the adsorption capacity of $\text{SiO}_2/\text{MnFe}_2\text{O}_4/\text{ZIF-8}$ toward MG dye. At a high pH value, the MG dye was deprotonated, while, at a low pH value, the MG dye was protonated. Thus, at a low pH value (2–5.5), the positively charged MG dye was electrically attracted to the negatively charged $\text{SiO}_2/\text{MnFe}_2\text{O}_4/\text{ZIF-8}$ (more –ve zeta potential, Figure 5e), while at

a higher pH value (8–12), the electrostatic repulsion between the negatively charged MG dye and negatively charged $\text{SiO}_2/\text{MnFe}_2\text{O}_4/\text{ZIF-8}$ surface caused a notable decrease in the adsorption capacity. For the adsorption of MR dye on the surface of $\text{SiO}_2/\text{MnFe}_2\text{O}_4/\text{ZIF-8}$ at different pH values, the adsorption capacity was constant until the pH of 5 and then decreased with the pH increase. This low adsorption capacity of MR anionic dye at $\text{pH} > 5$ was attributed to the repulsive forces between the negatively charged surface of $\text{SiO}_2/\text{MnFe}_2\text{O}_4/\text{ZIF-8}$ and the anionic dye.

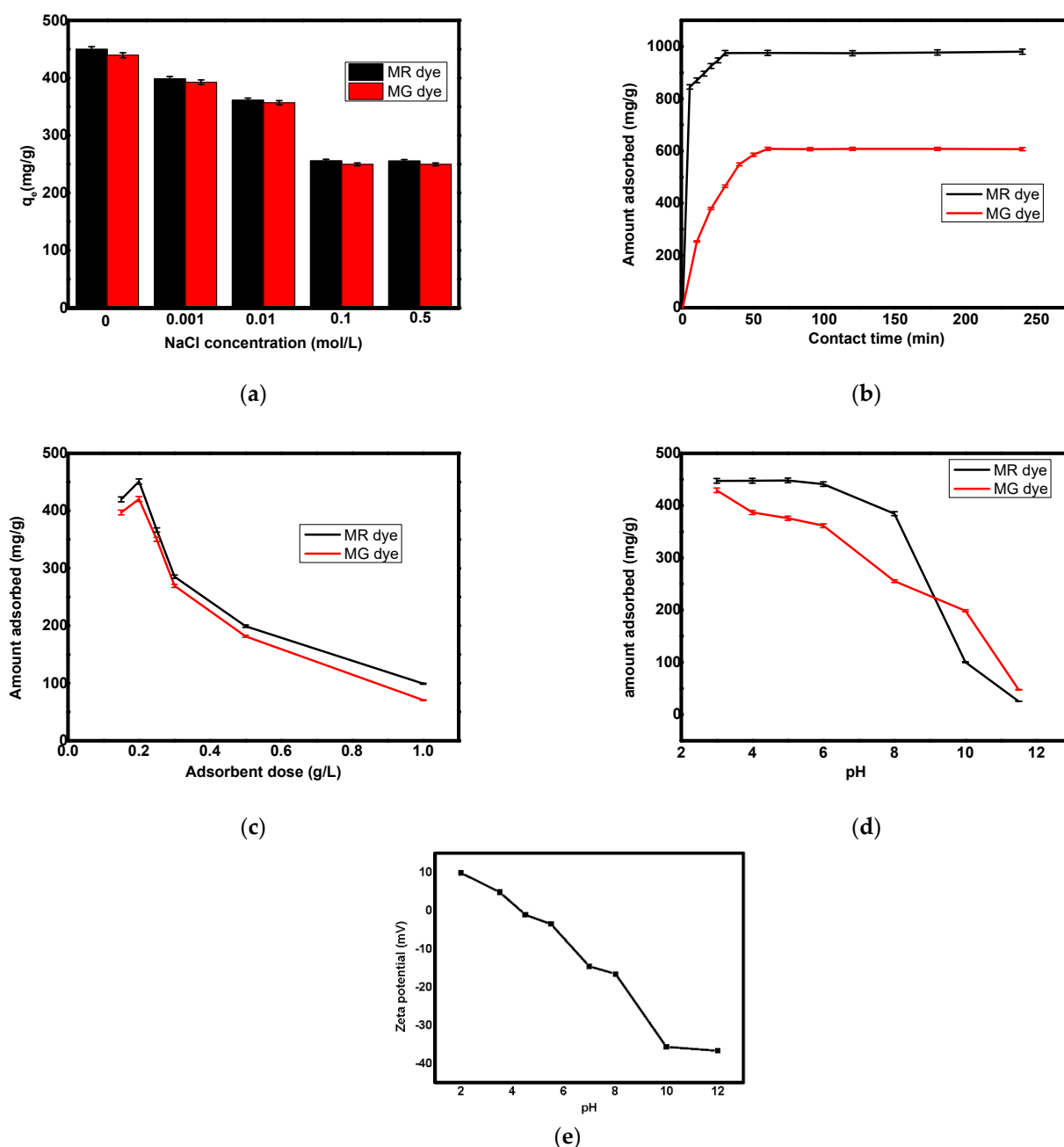


Figure 5. The effect of ionic strength (a), contact time (b), adsorbent dose (c), pH (d), and zeta potential measurements (e) on the removal of MR and MG dyes on the surface of $\text{SiO}_2/\text{MnFe}_2\text{O}_4/\text{ZIF-8}$.

3.3. Adsorption Isotherm

The mechanism of the adsorption process can be analyzed using isotherm studies [70,71]. In the current study, the adsorption of MG and MR dyes on the surface of the $\text{SiO}_2/\text{MnFe}_2\text{O}_4/\text{ZIF-8}$ nanocomposite was evaluated using the two familiar adsorption

models, Langmuir and Freundlich. The linear equations of Langmuir and Freundlich models are presented as shown in Equations (2) and (3), respectively.

$$\frac{C_e}{q_e} = \frac{1}{K_L q_m} + \frac{C_e}{q_m} \quad (2)$$

$$\text{Log} q_e = \frac{1}{n} \text{Log} C_e + \text{Log} K_F \quad (3)$$

where q_m , C_e , q_e , and K_L are the maximum adsorption capacity (mg/g), the concentration of dye at equilibrium (mg/L), the amount of the dye adsorbed at the equilibrium (mg/g), and the Langmuir adsorption constant (L/mg), respectively. K_F and n are constants of the Freundlich model that are related to the adsorption intensity and adsorption capacity, respectively. The linear plot of C_e and C_e/q_e according to the Langmuir model can be used for the determination of K_L and q_m from the slope and intercept, respectively. The linear plot of $\log C_e$ and $\log q_e$ according to the Freundlich model can be used for the determination of K_F and n from the intercept and slope, respectively. The fitting of experimental data for the adsorption of MG and MR dyes on the surface of the SiO₂/MnFe₂O₄/ZIF-8 nanocomposite using Langmuir and Freundlich models is shown in Figure 6. The calculated parameters of Langmuir and Freundlich isotherms are listed in Table 1.

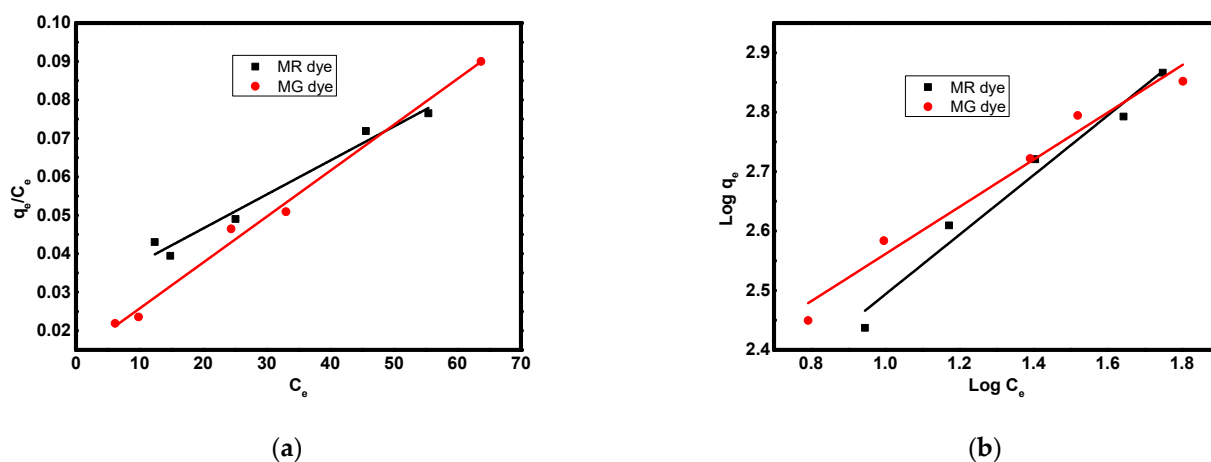


Figure 6. The fitting of experimental data to Langmuir isotherm (a) and Freundlich isotherm (b) for the adsorption of MG and MR dyes on the surface of SiO₂/MnFe₂O₄/ZIF-8 nanocomposite.

Table 1. The adsorption isotherm and kinetic parameters for the adsorption of MG and MR dyes on the surface of SiO₂/MnFe₂O₄/ZIF-8 nanocomposite.

| Dye | Langmuir | | | Freundlich | | | Pseudo-1st-Order | | | Pseudo-2nd-Order | | |
|-----|--------------|--------------|-------|------------|-----------------------------------|-------|----------------------------|---------|-------|------------------|--------|-------|
| | q_m (mg/g) | K_L (L/mg) | R^2 | $1/n$ | K_F (mg/g)(L/mg) ^{1/n} | R^2 | k_1 (min ⁻¹) | q_e | R^2 | k_2 (g/mg.h) | q_e | R^2 |
| MG | 1000.03 | 0.077 | 0.990 | 0.396 | 8.715 | 0.963 | 0.062 | 445.248 | 0.991 | 0.001 | 555.55 | 0.999 |
| MR | 1111.12 | 0.040 | 0.979 | 0.501 | 7.338 | 0.965 | 0.160 | 141.70 | 0.941 | 0.001 | 476.20 | 0.999 |

The Langmuir isotherm model states that the adsorbent surface is homogenous and all adsorption sites are energetically equivalent that can adsorb the adsorbate ions as a monolayer, while the Freundlich isotherm model states that the surface of the adsorbent is heterogeneous and the adsorption sites can adsorb the adsorbate ions as multilayers. The correlation coefficient (R^2) of the linear fit was used to evaluate the applicability of the model to describe the adsorption process. From the values of R^2 of the linear fit, the Langmuir isotherm was better at explaining the adsorption of both dyes MG and MR on the surface of the SiO₂/MnFe₂O₄/ZIF-8 nanocomposite. Moreover, the calculated q_m values were close to the experimental values. This means that the adsorption of MG and MR dyes

on the surface of the SiO₂/MnFe₂O₄/ZIF-8 nanocomposite was achieved via homogenous adsorption as a monolayer and confirmed the chemisorption mechanism.

The maximum adsorption capacities (q_m) for MR dye and MG dye are 1111.12 mg/g and 1000.03 mg/g, respectively. The Langmuir constant (K_L) indicates the degree of interactions between adsorbate ions and the adsorbent surface. In addition, the values of the Freundlich constant ($1/n$) indicate if the adsorption process is favored or not favored. For both dyes, $1/n$ values are less than 1, indicating the favorable adsorption of MG and MR dyes on the surface of the SiO₂/MnFe₂O₄/ZIF-8 nanocomposite. The results indicate the efficiency of the SiO₂/MnFe₂O₄/ZIF-8 nanocomposite as an adsorbent for wastewater treatment, especially after providing excellent results with two structurally different dyes with different electronic characteristics.

3.4. Adsorption Kinetics

For understanding the rate of dye removal from aqueous solution on the surface of the synthesized SiO₂/MnFe₂O₄/ZIF-8 nanocomposite, kinetic models were used to fit the experimental data of adsorption. In the present study, two kinetic models, pseudo-first-order and pseudo-second-order, were used to fit the experimental data of the MG and MR dyes adsorption on the surface of the SiO₂/MnFe₂O₄/ZIF-8 nanocomposite, as shown in Figure 7. The pseudo-first-order and pseudo-second-order kinetic models can be represented according to Equations (4) and (5), respectively.

$$\text{Log}(q_e - q_t) = \text{Log}q_e - \frac{k_1}{2.303}t \quad (4)$$

$$\frac{t}{q_t} = \frac{1}{k_2q_e^2} + \frac{t}{q_e} \quad (5)$$

where q_t , q_e , k_1 , and k_2 denote the adsorption amount at time t , the adsorption amount at equilibrium, the pseudo-first-order rate constant, and the pseudo-second-order rate constant, respectively.

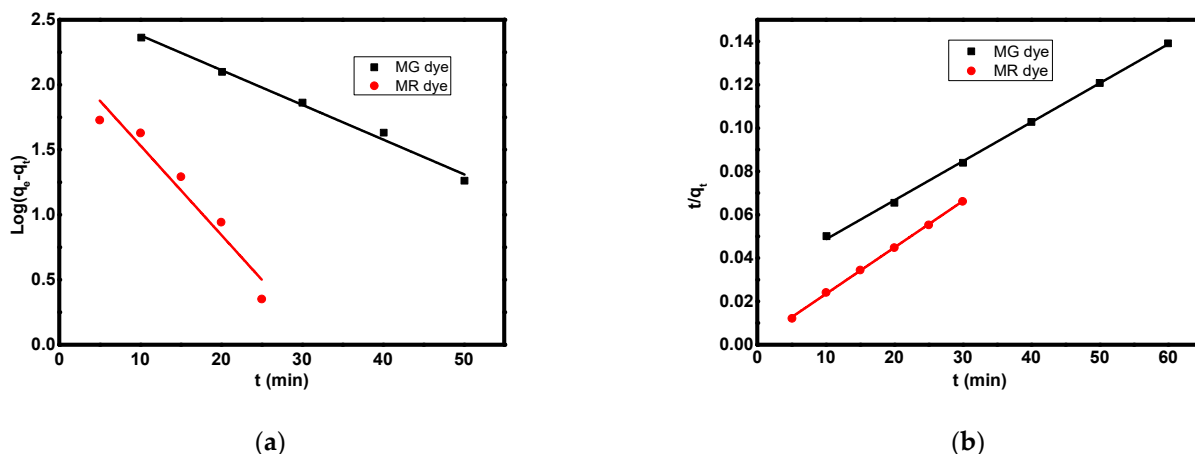


Figure 7. The fitting of experimental data to pseudo-first-order model (a) and pseudo-second-order (b) for the adsorption of MG and MR dyes on the surface of SiO₂/MnFe₂O₄/ZIF-8 nanocomposite.

The rate constants and coefficients of the pseudo-first-order model and pseudo-second-order model can be calculated from the plot of $\log(q_e - q_t)$ against t and t/q_t against t , respectively, as introduced in Figure 7a,b. The rate constants and coefficients of the pseudo-first-order model and pseudo-second-order model are listed in Table 1.

By comparing the correlation coefficient (R^2) values of the two kinetic models, the pseudo-second-order model had a higher R^2 value than the pseudo-first-order, indicating the greater suitability of the pseudo-second-order kinetic model to describe the adsorption of MG and MR dyes on the surface of the SiO₂/MnFe₂O₄/ZIF-8 nanocomposite. The

best fitting of experimental data to the pseudo-second-order kinetic models indicates the chemical interactions between dyes and the adsorbent surface during the adsorption process. Additionally, the calculated value of q_e from the pseudo-second-order model was found to be very close to the experimental value, confirming the greater suitability of the pseudo-second-order model for describing the adsorption of MG and MR dyes than the pseudo-first-order model. This means that the adsorption of MG and MR dyes on the surface of the $\text{SiO}_2/\text{MnFe}_2\text{O}_4/\text{ZIF-8}$ nanocomposite occurred via complicated chemical adsorption that may include many different interactions between the MG and MR dye molecules and the functional groups on the surface of $\text{SiO}_2/\text{MnFe}_2\text{O}_4/\text{ZIF-8}$.

3.5. Regeneration and Reusability Study

For the application of any adsorbent at an industrial scale, it is important to show good reusability results as the reusability of the adsorbent decreases the overall cost of the treatment. After the dye adsorption, the dye is required to be desorbed from the surface for the reactivation of adsorption sites for the next adsorption cycle. After each adsorption process, the adsorbent was collected using a magnet and the solution was examined for the presence of dyes. Then, the adsorbent was washed by the eluent to desorb the dyes for use in the next cycle. In the current study, the used eluent was a mixed solvent of ethyl alcohol and H_2O with a ratio of 8:2, respectively. This mixed solvent helps the desorption of MG and MR dyes from the surface of the $\text{SiO}_2/\text{MnFe}_2\text{O}_4/\text{ZIF-8}$ nanocomposite. Ethyl alcohol has a carbon chain that competes with the MG and MR dyes for the surface of the $\text{SiO}_2/\text{MnFe}_2\text{O}_4/\text{ZIF-8}$ nanocomposite and eases the desorption of dyes from the surface of the adsorbent. Ethyl alcohol also reduces the interaction between the dyes and the surface of the $\text{SiO}_2/\text{MnFe}_2\text{O}_4/\text{ZIF-8}$ nanocomposite. Additionally, H_2O helps the solubility of dyes and eases their desorption from the surface of the adsorbent. In the present study, the $\text{SiO}_2/\text{MnFe}_2\text{O}_4/\text{ZIF-8}$ nanocomposite was reused for the adsorption of MG and MR dyes for five successive cycles, as shown in Figure 8.

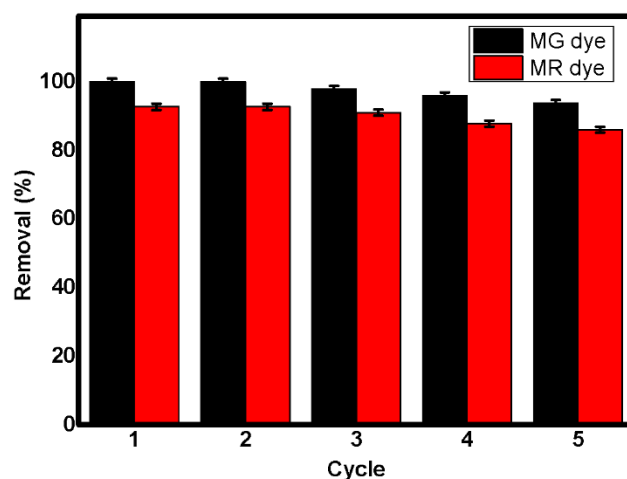


Figure 8. The reusability study of $\text{SiO}_2/\text{MnFe}_2\text{O}_4/\text{ZIF-8}$ nanocomposite for the removal of MG and MR dyes up to five cycles.

According to Figure 8, the highest removal efficiency (%) for both dyes on the surface of the $\text{SiO}_2/\text{MnFe}_2\text{O}_4/\text{ZIF-8}$ nanocomposite was achieved in the 1st cycle. This may be attributed to the availability of a large number of fresh active sites on the surface of the adsorbent to uptake large amounts of MG and MR dyes. The results showed the reduction in removal efficiencies to 93.5% and 86.5% for the removal of MG and MR dyes, respectively, after the 5th cycle. This decrease in the removal efficiency may be attributed to the damage of some adsorption sites and the blockage of the others due to the failure to desorb the dyes as a result of the strong interaction between MR and MG dyes and the surface of the $\text{SiO}_2/\text{MnFe}_2\text{O}_4/\text{ZIF-8}$ nanocomposite. The reusability results show that the prepared

SiO₂/MnFe₂O₄/ZIF-8 nanocomposite can be used many successive times for the removal of organic dyes from wastewater.

3.6. Comparative Study

To evaluate the efficiency of the synthesized SiO₂/MnFe₂O₄/ZIF-8 nanocomposite in the adsorption of MG and MR dyes, a comparative study of q_{max} of previously synthesized adsorbents used to remove MG and MR dyes is shown in Table 2.

Table 2. Comparison of SiO₂/MnFe₂O₄/ZIF-8 nanocomposite with previously reported adsorbents for the adsorption of MR and MG dyes.

| Adsorbent | Pollutant | Removal Capacity (mg/g) | Ref. |
|---|-----------|-------------------------|------------|
| SiO ₂ /MnFe ₂ O ₄ /ZIF-8 | MR | 1111.12 | This study |
| MIL-53 (Fe) DSAC | MR | 384.62 | [9] |
| K ₂ CO ₃ @activated carbon | MR | 226.90 | [72] |
| H ₃ PO ₄ @activated carbon | MR | 435.25 | [72] |
| 101(Fe)@PDopa@Fe ₃ O ₄ | MR | 625.0 | [73] |
| Woody biochar | MR | 156.25 | [74] |
| SiO ₂ /MnFe ₂ O ₄ /ZIF-8 | MG | 1000.03 | This study |
| Cu-MOFs/Fe ₃ O ₄ | MG | 125.15 | [75] |
| MIL-101-SO ₃ H | MG | 113.67 | [76] |
| 101(Fe)@Pdopa@Fe ₃ O ₄ | MG | 676 | [77] |
| TU-poly(AN-co-AA) | MG | 269.54 | [78] |
| AC@Fe ₂ O ₃ | MG | 311.40 | [79] |

According to Table 2, the classical adsorbents showed relatively low adsorption capacities toward MR and MG dyes, for example, carbon-based adsorbents such as K₂CO₃@activated carbon and woody biochar. However, carbon-based adsorbents were superior to other techniques for the removal of dyes from aqueous solution; the adsorption capacities ranged from 100 mg/g to 500 mg/g. Even after the magnetization of these carbon-based adsorbents, the adsorption capacity was improved but still low. For example, the magnetized activation carbon (AC@Fe₂O₃) gave an adsorption capacity of 311.40 mg/g. Previously, these adsorption capacities were considered to be high. The advancement of adsorbent synthesis using nanotechnology made these values low. Thus, the fabrication of advanced adsorbents such as magnetic MOFs (101(Fe)@PDopa@Fe₃O₄) provided an improved adsorption capacity exceeding 500 mg/g. These improved capacities were attributed to the large surface area, tunable pore size, composition diversity, and high selectivity. Compared to previously reported adsorbents, even the adsorbents of similar composition, the SiO₂/MnFe₂O₄/ZIF-8 nanocomposite showed good adsorption capacities toward the removal of MG and MR dyes, making it an effective promising adsorbent to remove organic dyes from wastewater.

4. Conclusions

In the present study, a good ternary adsorbent based on MOFs named SiO₂/MnFe₂O₄/ZIF-8 was synthesized with a very large surface area (831 m²·g⁻¹) and paramagnetic properties (23.7 emu·g⁻¹). The synthesized SiO₂/MnFe₂O₄/ZIF-8 nanocomposite was investigated for the adsorption of MG and MR dyes from an aqueous solution. The adsorption effective conditions were determined, including the effect of ionic strength, contact time, adsorbent dose, and pH. The fitting of adsorption data to isotherm models showed an agreement with the Langmuir model for the removal of both dyes, indicating that the dyes were adsorbed on the homogeneous surface of SiO₂/MnFe₂O₄/ZIF-8 as a monolayer. According to the Langmuir model, the adsorption capacities were 1111.12 mg/g and 1000.03 mg/g, for MR and MG, respectively. Additionally, the adsorption rate was investigated using the pseudo-first-order and pseudo-second-order models with an agreement to pseudo-first-order model indicating that the adsorption of both dyes

on the surface of the synthesized adsorbent was reached via chemisorption. In addition, the SiO₂/MnFe₂O₄/ZIF-8 nanocomposite can be used many successive times to remove organic dyes with high efficiency, helping decrease the treatment cost. The adsorption capacities of the SiO₂/MnFe₂O₄/ZIF-8 nanocomposite toward the removal of MG and MR dyes were compared to the other reported adsorbents showing higher values. Subsequently, the synthesized SiO₂/MnFe₂O₄/ZIF-8 nanocomposite is a promising material for the removal of coloring dyes from aqueous solutions and must be investigated for the removal of additional pollutants in the future.

Author Contributions: Conceptualization, M.A.T. and A.A.; methodology, A.A.; software, N.S.A.; validation, N.S.A. and H.O.; formal analysis, H.O.; investigation, H.O.; resources, A.A.; data curation, H.O.; writing—original draft preparation, A.A.; writing—review and editing, M.A.T.; visualization, A.A.; supervision, M.A.T.; project administration, A.A.; funding acquisition, N.S.A. All authors have read and agreed to the published version of the manuscript.

Funding: This research was funded by the Deanship of Scientific Research at King Khalid University under grant number RGP.2/182/43. Additionally, this research was funded by Princess Nourah bint Abdulrahman University Researchers Supporting Project number (PNURSP2022R19), Princess Nourah bint Abdulrahman University, Riyadh, Saudi Arabia.

Institutional Review Board Statement: Not applicable.

Informed Consent Statement: Not applicable.

Data Availability Statement: Not applicable.

Acknowledgments: The authors extend their appreciation to the Deanship of Scientific Research at King Khalid University for funding this work through the research groups program under grant number RGP.2/182/43. This research was also funded by Princess Nourah bint Abdulrahman University Researchers Supporting Project number (PNURSP2022R19), Princess Nourah bint Abdulrahman University, Riyadh, Saudi Arabia.

Conflicts of Interest: The authors declare no conflict of interest.

References

1. Qian, C.; Yin, J.; Zhao, J.; Li, X.; Wang, S.; Bai, Z.; Jiao, T. Facile preparation and highly efficient photodegradation performances of self-assembled Artemia eggshell-ZnO nanocomposites for wastewater treatment. *Colloids Surf. A Physicochem. Eng. Asp.* **2021**, *610*, 125752. [[CrossRef](#)]
2. Alzahrani, F.M.; Amari, A.; Katubi, K.M.; Alsaiari, N.S.; Tahoona, M.A. The synthesis of nanocellulose-based nanocomposites for the effective removal of hexavalent chromium ions from aqueous solution. *Open Chem.* **2022**, *20*, 970–983. [[CrossRef](#)]
3. Elgarahy, A.; Elwakeel, K.; Mohammad, S.; Elshoubaky, G. A critical review of biosorption of dyes, heavy metals and metalloids from wastewater as an efficient and green process. *Clean. Eng. Technol.* **2021**, *4*, 100209. [[CrossRef](#)]
4. Saravanan, A.; Kumar, P.S.; Jeevanantham, S.; Karishma, S.; Tajsabreen, B.; Yaashikaa, P.; Reshma, B. Effective water/wastewater treatment methodologies for toxic pollutants removal: Processes and applications towards sustainable development. *Chemosphere* **2021**, *280*, 130595. [[CrossRef](#)]
5. Rajoriya, S.; Saharan, V.K.; Pundir, A.S.; Nigam, M.; Roy, K. Adsorption of methyl red dye from aqueous solution onto eggshell waste material: Kinetics, isotherms and thermodynamic studies. *Curr. Res. Green Sustain. Chem.* **2021**, *4*, 100180. [[CrossRef](#)]
6. Verma, M.; Mitan, M.; Kim, H.; Vaya, D. Efficient photocatalytic degradation of Malachite green dye using facily synthesized cobalt oxide nanomaterials using citric acid and oleic acid. *J. Phys. Chem. Solids* **2021**, *155*, 110125. [[CrossRef](#)]
7. Bhardwaj, D.; Bharadvaja, N. Phycoremediation of effluents containing dyes and its prospects for value-added products: A review of opportunities. *J. Water Process Eng.* **2021**, *41*, 102080. [[CrossRef](#)]
8. Velusamy, S.; Roy, A.; Sundaram, S.; Kumar Mallick, T. A review on heavy metal ions and containing dyes removal through graphene oxide-based adsorption strategies for textile wastewater treatment. *Chem. Rec.* **2021**, *21*, 1570–1610. [[CrossRef](#)]
9. Ahmad, M.A.; Ahmad, N.; Bello, O.S. Modified durian seed as adsorbent for the removal of methyl red dye from aqueous solutions. *Appl. Water Sci.* **2015**, *5*, 407–423. [[CrossRef](#)]
10. Ismail, M.; Khan, M.; Khan, S.B.; Akhtar, K.; Khan, M.A.; Asiri, A.M. Catalytic reduction of picric acid, nitrophenols and organic azo dyes via green synthesized plant supported Ag nanoparticles. *J. Mol. Liq.* **2018**, *268*, 87–101. [[CrossRef](#)]
11. Shah, H.U.R.; Ahmad, K.; Naseem, H.A.; Parveen, S.; Ashfaq, M.; Rauf, A.; Aziz, T. Water stable graphene oxide metal-organic frameworks composite (ZIF-67@GO) for efficient removal of malachite green from water. *Food Chem. Toxicol.* **2021**, *154*, 112312. [[CrossRef](#)] [[PubMed](#)]

12. Naresh, G.; Malik, J.; Meena, V.; Mandal, T.K. pH-mediated collective and selective solar photocatalysis by a series of layered Aurivillius perovskites. *ACS Omega* **2018**, *3*, 11104–11116. [[CrossRef](#)] [[PubMed](#)]
13. Joseph, J.; Radhakrishnan, R.C.; Johnson, J.K.; Joy, S.P.; Thomas, J. Ion-exchange mediated removal of cationic dye-stuffs from water using ammonium phosphomolybdate. *Mater. Chem. Phys.* **2020**, *242*, 122488. [[CrossRef](#)]
14. Sahinkaya, E.; Tuncman, S.; Koc, I.; Guner, A.R.; Ciftci, S.; Aygun, A.; Sengul, S. Performance of a pilot-scale reverse osmosis process for water recovery from biologically-treated textile wastewater. *J. Environ. Manag.* **2019**, *249*, 109382. [[CrossRef](#)]
15. Bayat, M.; Javanbakht, V.; Esmaili, J. Synthesis of zeolite/nickel ferrite/sodium alginate bionanocomposite via a co-precipitation technique for efficient removal of water-soluble methylene blue dye. *Int. J. Biol. Macromol.* **2018**, *116*, 607–619. [[CrossRef](#)]
16. Amari, A.; Alzahrani, F.M.; Alsaiani, N.S.; Katubi, K.M.; Rebah, F.B.; Tahoon, M.A. Magnetic metal organic framework immobilized laccase for wastewater decolorization. *Processes* **2021**, *9*, 774. [[CrossRef](#)]
17. Kannaujia, R.; Prasad, V.; Rawat, P.; Rawat, V.; Thakur, A.; Majumdar, S.; Verma, M.; Rao, G.K.; Gupta, A.P.; Kumar, H. Facile synthesis of CuFe₂O₄ doped polyacrylic acid hydrogel nanocomposite and its application in dye degradation. *Mater. Lett.* **2019**, *252*, 198–201. [[CrossRef](#)]
18. Demissie, H.; An, G.; Jiao, R.; Ritigala, T.; Lu, S.; Wang, D. Modification of high content nanocluster-based coagulation for rapid removal of dye from water and the mechanism. *Sep. Purif. Technol.* **2021**, *259*, 117845. [[CrossRef](#)]
19. Mcyotto, F.; Wei, Q.; Macharia, D.K.; Huang, M.; Shen, C.; Chow, C.W. Effect of dye structure on color removal efficiency by coagulation. *Chem. Eng. J.* **2021**, *405*, 126674. [[CrossRef](#)]
20. Alsaiani, N.S.; Amari, A.; Katubi, K.M.; Alzahrani, F.M.; Rebah, F.B.; Tahoon, M.A. The Synthesis of Magnetic Nitrogen-Doped Graphene Oxide Nanocomposite for the Removal of Reactive Orange 12 Dye. *Adsorpt. Sci. Technol.* **2022**, *2022*, 9417542. [[CrossRef](#)]
21. Amari, A.; Elboughdiri, N.; Ghernaout, D.; Lajimi, R.H.; Alshahrani, A.M.; Tahoon, M.A.; Rebah, F.B. Multifunctional crosslinked chitosan/nitrogen-doped graphene quantum dot for wastewater treatment. *Ain Shams Eng. J.* **2021**, *12*, 4007–4014. [[CrossRef](#)]
22. Amari, A.; Alzahrani, F.M.; Mohammedsaleh Katubi, K.; Alsaiani, N.S.; Tahoon, M.A.; Rebah, F.B. Clay-polymer nanocomposites: Preparations and utilization for pollutants removal. *Materials* **2021**, *14*, 1365. [[CrossRef](#)] [[PubMed](#)]
23. Alsaiani, N.S.; Amari, A.; Katubi, K.M.; Alzahrani, F.M.; Rebah, F.B.; Tahoon, M.A. Innovative magnetite based polymeric nanocomposite for simultaneous removal of methyl orange and hexavalent chromium from water. *Processes* **2021**, *9*, 576. [[CrossRef](#)]
24. Shahadat, M.; Isamil, S. Regeneration performance of clay-based adsorbents for the removal of industrial dyes: A review. *RSC Adv.* **2018**, *8*, 24571–24587.
25. Gao, X.; Zhang, Y.; Dai, Y.; Fu, F. High-performance magnetic carbon materials in dye removal from aqueous solutions. *J. Solid State Chem.* **2016**, *239*, 265–273. [[CrossRef](#)]
26. Qiao, D.; Li, Z.; Duan, J.; He, X. Adsorption and photocatalytic degradation mechanism of magnetic graphene oxide/ZnO nanocomposites for tetracycline contaminants. *Chem. Eng. J.* **2020**, *400*, 125952. [[CrossRef](#)]
27. Okoli, C.P.; Ofomaja, A.E. Development of sustainable magnetic polyurethane polymer nanocomposite for abatement of tetracycline antibiotics aqueous pollution: Response surface methodology and adsorption dynamics. *J. Clean. Prod.* **2019**, *217*, 42–55. [[CrossRef](#)]
28. Mittal, H.; Alhassan, S.M.; Ray, S.S. Efficient organic dye removal from wastewater by magnetic carbonaceous adsorbent prepared from corn starch. *J. Environ. Chem. Eng.* **2018**, *6*, 7119–7131. [[CrossRef](#)]
29. Nasseh, N.; Arghavan, F.S.; Rodriguez-Couto, S.; Hossein Panahi, A. Synthesis of FeNi₃/SiO₂/CuS magnetic nano-composite as a novel adsorbent for Congo Red dye removal. *Int. J. Environ. Anal. Chem.* **2022**, *102*, 2342–2362. [[CrossRef](#)]
30. Alzahrani, F.M.; Alsaiani, N.S.; Katubi, K.M.; Amari, A.; Ben Rebah, F.; Tahoon, M.A. Synthesis of polymer-based magnetic nanocomposite for multi-pollutants removal from water. *Polymers* **2021**, *13*, 1742. [[CrossRef](#)]
31. Jiang, C.; Wang, X.; Qin, D.; Da, W.; Hou, B.; Hao, C.; Wu, J. Construction of magnetic lignin-based adsorbent and its adsorption properties for dyes. *J. Hazard. Mater.* **2019**, *369*, 50–61. [[CrossRef](#)] [[PubMed](#)]
32. Yang, J.; Yang, Y.W. Metal-organic frameworks for biomedical applications. *Small* **2020**, *16*, 1906846. [[CrossRef](#)] [[PubMed](#)]
33. Liu, L.; Zhou, Y.; Liu, S.; Xu, M. The applications of metal-organic frameworks in electrochemical sensors. *ChemElectroChem* **2018**, *5*, 6–19. [[CrossRef](#)]
34. Bavykina, A.; Kolobov, N.; Khan, I.S.; Bau, J.A.; Ramirez, A.; Gascon, J. Metal-organic frameworks in heterogeneous catalysis: Recent progress, new trends, and future perspectives. *Chem. Rev.* **2020**, *120*, 8468–8535. [[CrossRef](#)]
35. Ahmadijokani, F.; Mohammadkhani, R.; Ahmadipouya, S.; Shokrgozar, A.; Rezakazemi, M.; Molavi, H.; Aminabhavi, T.M.; Arjmand, M. Superior chemical stability of UiO-66 metal-organic frameworks (MOFs) for selective dye adsorption. *Chem. Eng. J.* **2020**, *399*, 125346. [[CrossRef](#)]
36. Gu, Q.; Ng, H.Y.; Zhao, D.; Wang, J. Metal-Organic Frameworks (MOFs)-boosted filtration membrane technology for water sustainability. *APL Mater.* **2020**, *8*, 040902. [[CrossRef](#)]
37. Iman, K.; Shahid, M.; Khan, M.S.; Ahmad, M.; Sama, F. Topology, magnetism and dye adsorption properties of metal organic frameworks (MOFs) synthesized from bench chemicals. *CrystEngComm* **2019**, *21*, 5299–5309. [[CrossRef](#)]
38. Yin, H.-Q.; Yin, X.-B. Metal-organic frameworks with multiple luminescence emissions: Designs and applications. *Acc. Chem. Res.* **2020**, *53*, 485–495. [[CrossRef](#)]

39. Tung, T.T.; Tran, M.T.; Feller, J.-F.; Castro, M.; Van Ngo, T.; Hassan, K.; Nine, M.J.; Losic, D. Graphene and metal organic frameworks (MOFs) hybridization for tunable chemoresistive sensors for detection of volatile organic compounds (VOCs) biomarkers. *Carbon* **2020**, *159*, 333–344. [[CrossRef](#)]
40. Connolly, B.M.; Madden, D.G.; Wheatley, A.E.; Fairen-Jimenez, D. Shaping the future of fuel: Monolithic metal–organic frameworks for high-density gas storage. *J. Am. Chem. Soc.* **2020**, *142*, 8541–8549. [[CrossRef](#)]
41. Gao, W.; Li, X.; Zhang, X.; Su, S.; Luo, S.; Huang, R.; Jing, Y.; Luo, M. Photocatalytic nitrogen fixation of metal–organic frameworks (MOFs) excited by ultraviolet light: Insights into the nitrogen fixation mechanism of missing metal cluster or linker defects. *Nanoscale* **2021**, *13*, 7801–7809. [[CrossRef](#)] [[PubMed](#)]
42. Kumar, P.; Pournara, A.; Kim, K.-H.; Bansal, V.; Rapti, S.; Manos, M.J. Metal-organic frameworks: Challenges and opportunities for ion-exchange/sorption applications. *Prog. Mater. Sci.* **2017**, *86*, 25–74. [[CrossRef](#)]
43. Lawson, H.D.; Walton, S.P.; Chan, C. Metal–Organic Frameworks for Drug Delivery: A Design Perspective. *ACS Appl. Mater. Interfaces* **2021**, *13*, 7004–7020. [[CrossRef](#)]
44. Liu, X.; Liu, Y. Recent progress in the design and synthesis of zeolite-like metal–organic frameworks (ZMOFs). *Dalton Trans.* **2021**, *50*, 3450–3458. [[CrossRef](#)] [[PubMed](#)]
45. Long, J.R.; Yaghi, O.M. The pervasive chemistry of metal–organic frameworks. *Chem. Soc. Rev.* **2009**, *38*, 1213–1214. [[CrossRef](#)]
46. Férey, G. Hybrid porous solids: Past, present, future. *Chem. Soc. Rev.* **2008**, *37*, 191–214. [[CrossRef](#)]
47. Lu, X.F.; Fang, Y.; Luan, D.; Lou, X.W.D. Metal–organic frameworks derived functional materials for electrochemical energy storage and conversion: A mini review. *Nano Lett.* **2021**, *21*, 1555–1565. [[CrossRef](#)]
48. Anand, B.; Kim, K.-H.; Sonwani, R.K.; Szulejko, J.E.; Heynderickx, P.M. Removal of gaseous benzene by a fixed-bed system packed with a highly porous metal-organic framework (MOF-199) coated glass beads. *Environ. Res.* **2022**, *208*, 112655. [[CrossRef](#)]
49. Bayazit, Ş.S.; Yildiz, M.; Aşçi, Y.S.; Şahin, M.; Bener, M.; Eğlence, S.; Salam, M.A. Rapid adsorptive removal of naphthalene from water using graphene nanoplatelet/MIL-101 (Cr) nanocomposite. *J. Alloys Compd.* **2017**, *701*, 740–749. [[CrossRef](#)]
50. Uddin, M.J.; Ampiauw, R.E.; Lee, W. Adsorptive removal of dyes from wastewater using a metal-organic framework: A review. *Chemosphere* **2021**, *284*, 131314. [[CrossRef](#)]
51. Zhang, H.-Y.; Yang, C.; Geng, Q.; Fan, H.-L.; Wang, B.-J.; Wu, M.-M.; Tian, Z. Adsorption of hydrogen sulfide by amine-functionalized metal organic framework (MOF-199): An experimental and simulation study. *Appl. Surf. Sci.* **2019**, *497*, 143815. [[CrossRef](#)]
52. Hamed, A.; Zarandi, M.B.; Nateghi, M.R. Highly efficient removal of dye pollutants by MIL-101(Fe) metal-organic framework loaded magnetic particles mediated by Poly L-Dopa. *J. Environ. Chem. Eng.* **2019**, *7*, 102882. [[CrossRef](#)]
53. Li, W.; Wu, X.; Li, S.; Tang, W.; Chen, Y. Magnetic porous Fe₃O₄/carbon octahedra derived from iron-based metal-organic framework as heterogeneous Fenton-like catalyst. *Appl. Surf. Sci.* **2018**, *436*, 252–262. [[CrossRef](#)]
54. Alzahrani, F.M.; Alsaiani, N.S.; Katubi, K.M.; Amari, A.; Tahooon, M.A. Synthesis, characterization, and application of magnetized lanthanum (III)-based metal-organic framework for the organic dye removal from water. *Adsorpt. Sci. Technol.* **2022**, *2022*, 3513829. [[CrossRef](#)]
55. Mahmoodi, N.M.; Arabloo, M.; Abdi, J. Laccase immobilized manganese ferrite nanoparticle: Synthesis and LSSVM intelligent modeling of decolorization. *Water Res.* **2014**, *67*, 216–226. [[CrossRef](#)]
56. Stöber, W.; Fink, A.; Bohn, E. Controlled growth of monodisperse silica spheres in the micron size range. *J. Colloid Interface Sci.* **1968**, *26*, 62–69. [[CrossRef](#)]
57. Li, N.; Fu, F.; Lu, J.; Ding, Z.; Tang, B.; Pang, J. Facile preparation of magnetic mesoporous MnFe₂O₄@ SiO₂–CTAB composites for Cr (VI) adsorption and reduction. *Environ. Pollut.* **2017**, *220*, 1376–1385. [[CrossRef](#)]
58. Abdi, J.; Vossoughi, M.; Mahmoodi, N.M.; Alemzadeh, I. Synthesis of metal-organic framework hybrid nanocomposites based on GO and CNT with high adsorption capacity for dye removal. *Chem. Eng. J.* **2017**, *326*, 1145–1158. [[CrossRef](#)]
59. Laokul, P.; Amornkitbamrung, V.; Seraphin, S.; Maensiri, S. Characterization and magnetic properties of nanocrystalline CuFe₂O₄, NiFe₂O₄, ZnFe₂O₄ powders prepared by the Aloe vera extract solution. *Curr. Appl. Phys.* **2011**, *11*, 101–108. [[CrossRef](#)]
60. Mahmoodi, N.M. Manganese ferrite nanoparticle: Synthesis, characterization, and photocatalytic dye degradation ability. *Desalination Water Treat.* **2015**, *53*, 84–90. [[CrossRef](#)]
61. Bustamante, E.L.; Fernández, J.L.; Zamaro, J.M. Influence of the solvent in the synthesis of zeolitic imidazolate framework-8 (ZIF-8) nanocrystals at room temperature. *J. Colloid Interface Sci.* **2014**, *424*, 37–43. [[CrossRef](#)] [[PubMed](#)]
62. Hu, Y.; Kazemian, H.; Rohani, S.; Huang, Y.; Song, Y. In situ high pressure study of ZIF-8 by FTIR spectroscopy. *Chem. Commun.* **2011**, *47*, 12694–12696. [[CrossRef](#)] [[PubMed](#)]
63. Kumar, R.; Jayaramulu, K.; Maji, T.K.; Rao, C. Hybrid nanocomposites of ZIF-8 with graphene oxide exhibiting tunable morphology, significant CO₂ uptake and other novel properties. *Chem. Commun.* **2013**, *49*, 4947–4949. [[CrossRef](#)] [[PubMed](#)]
64. Yang, L.-X.; Wang, F.; Meng, Y.-F.; Tang, Q.-H.; Liu, Z.-Q. Fabrication and characterization of manganese ferrite nanospheres as a magnetic adsorbent of chromium. *J. Nanomater.* **2013**, *2013*, 2. [[CrossRef](#)]
65. Zeng, F.; He, Y.; Lian, Z.; Xu, J. The impact of solution chemistry of electrolyte on the sorption of pentachlorophenol and phenanthrene by natural hematite nanoparticles. *Sci. Total Environ.* **2014**, *466*, 577–585. [[CrossRef](#)] [[PubMed](#)]
66. Noreen, S.; Bhatti, H.N.; Iqbal, M.; Hussain, F.; Sarim, F.M. Chitosan, starch, polyaniline and polypyrrole biocomposite with sugarcane bagasse for the efficient removal of Acid Black dye. *Int. J. Biol. Macromol.* **2020**, *147*, 439–452. [[CrossRef](#)] [[PubMed](#)]

67. Tahir, N.; Bhatti, H.N.; Iqbal, M.; Noreen, S. Biopolymers composites with peanut hull waste biomass and application for Crystal Violet adsorption. *Int. J. Biol. Macromol.* **2017**, *94*, 210–220. [[CrossRef](#)]
68. Bayomie, O.S.; Kandeel, H.; Shoeib, T.; Yang, H.; Youssef, N.; El-Sayed, M.M. Novel approach for effective removal of methylene blue dye from water using fava bean peel waste. *Sci. Rep.* **2020**, *10*, 7824. [[CrossRef](#)]
69. Bellahsen, N.; Varga, G.; Halyag, N.; Kertész, S.; Tombácz, E.; Hodúr, C. Pomegranate peel as a new low-cost adsorbent for ammonium removal. *Int. J. Environ. Sci. Technol.* **2021**, *18*, 711–722. [[CrossRef](#)]
70. Saxena, M.; Sharma, N.; Saxena, R. Highly efficient and rapid removal of a toxic dye: Adsorption kinetics, isotherm, and mechanism studies on functionalized multiwalled carbon nanotubes. *Surf. Interfaces* **2020**, *21*, 100639. [[CrossRef](#)]
71. Wang, J.; Guo, X. Adsorption isotherm models: Classification, physical meaning, application and solving method. *Chemosphere* **2020**, *258*, 127279. [[CrossRef](#)] [[PubMed](#)]
72. Khan, E.A.; Khan, T.A. Adsorption of methyl red on activated carbon derived from custard apple (*Annona squamosa*) fruit shell: Equilibrium isotherm and kinetic studies. *J. Mol. Liq.* **2018**, *249*, 1195–1211. [[CrossRef](#)]
73. Dadfarnia, S.; Shabani, A.H.; Moradi, S.; Emami, S. Methyl red removal from water by iron based metal-organic frameworks loaded onto iron oxide nanoparticle adsorbent. *Appl. Surf. Sci.* **2015**, *330*, 85–93. [[CrossRef](#)]
74. Ding, G.; Wang, B.; Chen, L.; Zhao, S. Simultaneous adsorption of methyl red and methylene blue onto biochar and an equilibrium modeling at high concentration. *Chemosphere* **2016**, *163*, 283–289. [[CrossRef](#)]
75. Liu, H.; Mo, Z.; Li, L.; Chen, F.; Wu, Q.; Qi, L. Efficient removal of copper (II) and malachite green from aqueous solution by magnetic magnesium silicate composite. *J. Chem. Eng. Data* **2017**, *62*, 3036–3042. [[CrossRef](#)]
76. Shi, Z.; Xu, C.; Guan, H.; Li, L.; Fan, L.; Wang, Y.; Liu, L.; Meng, Q.; Zhang, R. Magnetic metal organic frameworks (MOFs) composite for removal of lead and malachite green in wastewater. *Colloids Surf. A Physicochem. Eng. Asp.* **2018**, *539*, 382–390. [[CrossRef](#)]
77. Luo, X.-P.; Fu, S.-Y.; Du, Y.-M.; Guo, J.-Z.; Li, B. Adsorption of methylene blue and malachite green from aqueous solution by sulfonic acid group modified MIL-101. *Microporous Mesoporous Mater.* **2017**, *237*, 268–274. [[CrossRef](#)]
78. Adeyi, A.A.; Jamil, S.N.; Abdullah, L.C.; Choong, T.S. Adsorption of malachite green dye from liquid phase using hydrophilic thiourea-modified poly (acrylonitrile-co-acrylic acid): Kinetic and isotherm studies. *J. Chem.* **2019**, *2019*, 4321475. [[CrossRef](#)]
79. Altıntig, E.; Onaran, M.; Sari, A.; Altundag, H.; Tuzen, M. Preparation, characterization and evaluation of bio-based magnetic activated carbon for effective adsorption of malachite green from aqueous solution. *Mater. Chem. Phys.* **2018**, *220*, 313–321. [[CrossRef](#)]